Electronic Band Structure Changes across the Antiferromagnetic Phase Transition of Exfoliated $MnPS_3$ Flakes Probed by μ-ARPES

Jeff Strasdas, Benjamin Pestka, Miłosz Rybak, Adam K. Budniak, Niklas Leuth, Honey Boban, Vitaliy Feyer, Iulia Cojocariu, Daniel Baranowski, José Avila, Pavel Dudin, Aaron Bostwick, Chris Jozwiak, Eli Rotenberg, Carmine Autieri, Yaron Amouyal, Lukasz Plucinski, Efrat Lifshitz, Magdalena Birowska, and Markus Morgenstern*

ABSTRACT: Exfoliated magnetic 2D materials enable versatile tuning of magnetization, e.g., by gating or providing proximity-induced exchange interaction. However, their electronic band structure after exfoliation has not been probed, presumably due to their photochemical sensitivity. Here, we provide micrometer-scale angle-resolved photoelectron spectroscopy of the exfoliated intralayer antiferromagnet $MnPS_3$ above and below the Néel temperature down to one monolayer. Favorable comparison with density functional theory calculations enables identifying the orbital character of the observed bands. Consistently, we find pronounced changes across the Néel temperature for bands consisting of Mn 3d and 3p levels of adjacent S atoms. The deduced orbital mixture indicates that the superexchange is relevant for the magnetic interaction. There are only minor changes between monolayer and thicker films, demonstrating the predominant 2D character of $MnPS_3$. The novel access is transferable to other MPX_3 materials (M: transition metal, P: phosphorus, X: chalcogenide), providing several antiferromagnetic arrangements.

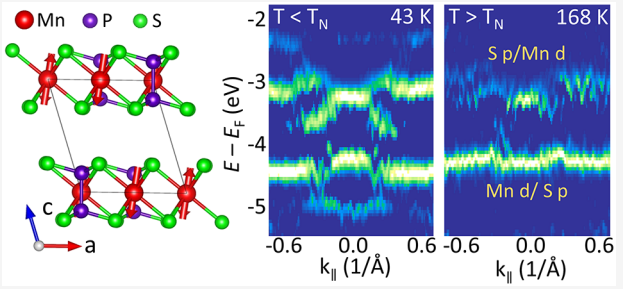

KEYWORDS: *magnetic 2D materials, angular resolved photoelectron spectroscopy, layered magnetism, μ-ARPES, density functional theory*

The first successful exfoliation of CrI_3,[1] $Cr_2Ge_2Te_6$,[2] and other layered magnetic materials[3−7] added ferro- and antiferromagnets to the toolbox of exfoliation-based heterostructures.[8] This enabled several magnetoelectric effects such as deliberate gate tuning of the spin-flop transition[9,10] from antiferro- to ferrimagnetism[11] or from ferro- to paramagnetism.[12] Moreover, the exchange coupling of the ferromagnet was successfully transferred via proximity to neighboring 2D materials[13] such as graphene,[14−16] WSe_2,[17] the topological insulator WTe_2,[18] and the superconductor $NbSe_2$.[19−21] Recently, also twisted layers of 2D antiferromagnets exhibited distinct magnetic properties from their regularly stacked counterparts.[22−24]

Nevertheless, the basic electronic band structure of exfoliated 2D magnetic materials has never been probed. Previous angularly resolved photoelectron spectroscopy (ARPES) data have only been obtained on in situ cleaved bulk materials[22,27−36] or in situ after molecular beam epitaxy (MBE).[37] Consequently, the intralayer antiferromagnetic insulators MPS_3 (M = Mn, Fe, Co, Ni)[38−40] have not been probed across the phase transition, since the relatively large band gaps prohibit low-temperature ARPES of cleaved crystals[36,41,42] (Supplementary Section S1.K). Moreover, the complex structure has not enabled MBE so far. Interestingly, MPS_3 materials feature rather strong magnetoelastic,[43,44] magnetoelectric,[45−49] and magnetically induced electron−phonon[50] couplings as well as appealing optical properties,[51−54] all directly related to the band structure.

Here, we investigate exfoliated $MnPS_3$, an intralayer antiferromagnet (AFM) with a honeycomb-type Néel order of Mn^{2+} ions (Figure 1a).[45,55−57] The AFM order persists down to a monolayer.[43,58−60] The interlayer exchange interaction is weakly ferromagnetic,[61] breaking inversion symmetry and, hence, enabling magnetoelectric coupling[45,47] This has been exploited to image the AFM domains (∼100 μm)[62] and to determine the critical exponent β = 0.37 using second harmonic generation.[47,63] The Néel temperature of the bulk material is T_N = 78 K.[56,64] The optical band gap is 2.94 eV at T = 5 K[65,66] with additional localized inter-d-level transitions at lower excitation energies.[65] Weak interlayer van der Waals

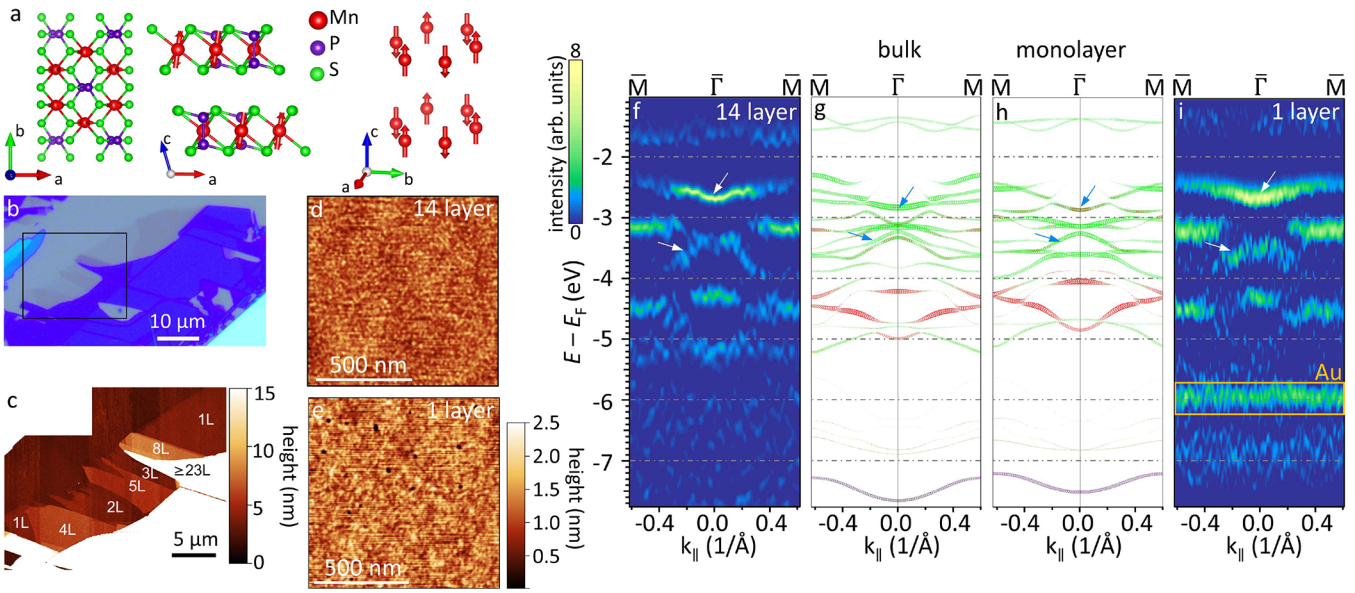

Figure 1. Exfoliation and comparison of monolayer and bulk. (a) Atomic and magnetic structure of $MnPS_3$ with Mn magnetic moments depicted as arrows. Left: top view, middle: side view of two layers, right: perspective view with Mn atoms only (Graphics are produced with the VESTA program[25]). (b) Optical microscope image of a thick flake (violet) with several few-layer flakes at the upper left rim (darker gray areas) exfoliated on Au/Ti/SiO_2/Si. (c) Tapping-mode atomic force microscopy (AFMi) image of the highlighted area in (b) with layer thicknesses marked. (d, e) Tapping mode AFMi images of areas probed by ARPES in (f) and (i), RMS roughness: 0.24 nm (d), 0.30 nm (e). (f) Curvature plot of ARPES data for 14 layers of $MnPS_3$, T = 7 K, and photon energy $h\nu$ = 100 eV. (g) Band structure from DFT+U for bulk $MnPS_3$ along the same $k_\parallel$ direction as in f, a rigid shift adapts the upper valence band to the highest energy band of the ARPES data in (f), k_z = 0.46 Å, U = 1.8 eV. Only bands with s, p_z, and d_{z^2} contribution are displayed as required by the ARPES selection rules[26] (Supplementary Section S1.J). The band structure with all bands is shown in Figure 2c. The colors mark the dominating orbital (red: Mn $3d_{z^2}$, green: S $3p_z$, violet: P $3p_z$). The symbol size indicates the strength of the dominating orbital with respect to the other orbitals that contribute to the state (Supplementary Section S6). (h) Same as (g) but for a monolayer. (i) Same as (f) but for an area with the thickness of 1 layer. The band marked Au is due to a Au 5d band of the substrate (Supplementary Section S1.G). Arrows in parts (f) and (i) mark bands discussed in the text. The energy scale in (f) belongs to (f)−(i).

binding with energy density 0.25 J/m^2 (graphene: 0.38 J/m^2) enables exfoliation.[66]

Here, we employ such exfoliation down to single layers onto a Au/Ti-covered Si/SiO_2 substrate. We probe the insulating material with μ-ARPES above and below T_N. We find excellent agreement with density functional theory (DFT+U) calculations enabling one to deduce an adequate U = 1.8 eV and to assign the orbital character of the observed bands. The most pronounced changes across T_N appear for an occupied band dominated by Mn 3d orbitals, with additional contributions from the adjacent S 3p orbitals. Weaker changes are found for less strongly bound bands dominated by S 3p orbitals with contributions from Mn 3d levels. These changes are qualitatively reproduced by DFT+U comparing the AFM Néel and the paramagnetic (PM) phase. The changes are attributed to an influence of both direct Mn−Mn exchange and a superexchange that, in turn, lead to a modification of the orbital mixture and the dispersion of the bands. The band structure remains similar down to the thickness of 1 layer evidencing the strong 2D character of the material.

The exfoliation of $MnPS_3$ typically leads to thick flakes with thin layers down to a monolayer at their rim (Figure 1b,c).[66] We found that direct exfoliation after plasma ashing of the Au substrate provides a higher yield of thin areas, e.g., a two layer thick area with size of 150 × 300 μm^2 (Supplementary Section S1.B).

The areas of different thicknesses at the same flake (Figure 1c) are advantageous for μ-ARPES providing a focus down to 5 μm in diameter.[67] Hence, we could probe multiple thicknesses down to the monolayer partially on the same flake. Extremely thick flakes (>1000 layers) were impossible to probe due to charging effects, evidencing the insulating character of the material (Supplementary Section S1.K). Figure 1f,i displays curvature plots of the recorded ARPES data along $\overline{\mathrm{M\Gamma M}}$ for a relatively thick bulk-type area and a monolayer area, both below T_N and recorded with the same ARPES parameters. The apparent bands are quite similar for the different thicknesses. This reveals that the mutual interaction of the van der Waals type between the layers has a minor impact on the electronic properties. Hence, the bulk material is also predominantly a 2D-type magnet.

For comparison, the bands from the DFT+U calculations (Supplementary Section S2) are displayed in Figure 1g,h. The only adaption to the ARPES data is a rigid energy shift such that the valence band maximum $E_{\mathrm{VBM}}^{\overline{\mathrm{M\Gamma M}}}$ in the $\overline{\mathrm{M\Gamma M}}$ direction is aligned with the highest energy band visible in ARPES. This alignment is done once and then kept for all figures comparing experimental and theoretical data. It reveals $E_F - E_{\mathrm{VBM}}^{\overline{\mathrm{M\Gamma M}}}$ = 1.6 eV (1.7 eV) for bulk (monolayer) with respect to the measured Fermi level E_F on Au (Supplementary Section S1.E). Accordingly, we use $E - E_F$ for all comparative experimental and theoretical data. Moreover, we show only the bands with orbital characters that lead to a strong ARPES matrix element[26] (Supplementary Section S1.J, full band structure: Figure 2c). This unbiased selection gives very good agreement with the experimental data. Minor changes in the measured band structure are interestingly reproduced by the calculations (arrows in Figure 1f−i). For example, the nearly parabolic part of the band at $E - E_F \simeq -2.8$ eV (−3.1 eV) is more curved around $\overline{\Gamma}$ for one layer in the experiment (calculation).

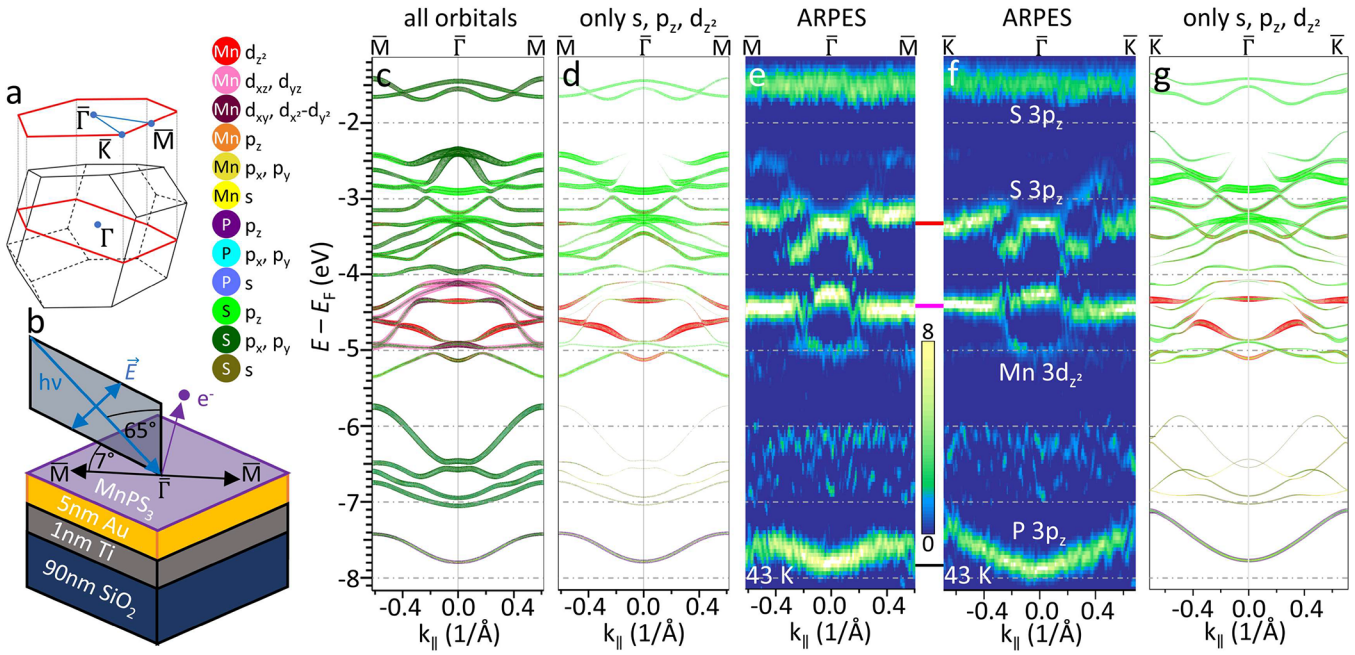

Figure 2. Electronic structure of $MnPS_3$ with the AFM-Néel phase. (a) The first Brillouin zone (BZ) of the monolayer (red) and of the bulk (black), with the red plane within the bulk BZ marking the projection of the surface BZ. (b) Sample sequence (on top of a Si substrate) and photon beam geometry with the polarization direction $\vec{E}$ in the plane of incidence. (c, d) Band structure obtained within the DFT+U approach (U = 1.8 eV, k_z = 0.0/Å). The electronic states are color-coded by their atomic orbital contribution with size, giving the contribution strength (color code on the left). (c) All bands. (d) Only bands with s, p_z, and d_{z^2} contribution as required by the ARPES selection rules[26] (Supplementary Section S1.J). (e) Curvature plot of ARPES data along $\overline{M\Gamma M}$ below T_N, T = 43 K, $h\nu$ = 50 eV, and 62 layers. (f) Same as (e) along $\overline{K\Gamma K}$. Dominating orbitals according to d are marked. Colored lines between parts (e) and (f) refer to Figure 3. (g) Same as (d) along $\overline{K\Gamma K}$. The energy scale in (c) belongs to (c)–(g).

Moreover, the bands propagating downward from $\bar{\Gamma}$ at $E - E_F \simeq -3.6$ eV are steeper for the thick film in both panels. This indicates a convincing agreement between ARPES and DFT+U data or, in turn, an adequate choice of the parameters U and k_z (the wave vector perpendicular to the surface) as deduced by detailed comparison (Supplementary Section S4). Eventually, it demonstrates the appropriateness of DFT+U to describe $MnPS_3$ adequately, as discussed in more detail below.

Due to the small differences between monolayer and bulk, we concentrate on the thicker layers in the following. In order to identify the orbital character of the probed bands below T_N, a comparison between the ARPES data at T = 43 K and the bands from the DFT+U approach with the AFM-Néel phase is discussed. Figure 2e,f shows the measured band structure of thick $MnPS_3$ (62 layers) along the $\overline{M\Gamma M}$ and the $\overline{K\Gamma K}$ direction below T_N = 78 K recorded at photon energy $h\nu$ = 50 eV. This $h\nu$ is chosen to hit the Mn 3p → 3d resonance for a better visibility of Mn-related bands (Supplementary Section S1.I). The AFM-Néel band structure calculated by DFT+U is displayed in Figure 2c,d,g with marked orbital contributions. A detailed analysis of characteristic features that monotonously change with U enabled us to select the proper U = 1.8 eV (Supplementary Section S4.A). Changes in the band structure with k_z are more subtle. The best agreement for $h\nu$ = 50 eV is found at $k_z \simeq 0.0$/Å (Supplementary Section S4.B), also leading to a reasonable match with the k_z dispersion deduced from photon energy dependent ARPES (Supplementary Section S5). Since matrix elements in our experimental geometry (Figure 2b) select s-type, p_z-type, and d_{z^2}-type states (Supplementary Section S1.J), we also plot the DFT+U results including only bands with these contributions (Figure 2d,g). Such band selection provides rather good agreement with the experimental data. Moreover, the comparison identifies the orbital contribution that dominates the four strongest groups of bands in the ARPES data, as indicated in Figure 2f. All of these bands have additional contributions from other orbitals (Supplementary Section S6). The band labeled P $3p_z$ has significant contributions from S 3p orbitals, the bands labeled Mn $3d_{z^2}$ consist of all Mn 3d levels and weaker contributions from all S 3p orbitals, and the two blocks of bands labeled S $3p_z$ have contributions from the other S 3p orbitals and weaker contributions from Mn 3d levels. This demonstrates that all these orbitals are significantly involved in the hybridization, i.e., in the bonding within $MnPS_3$. In particular, the strong mixing of the Mn 3d and S 3p levels implies their combined involvement as required for the superexchange interaction.

To corroborate the good agreement between ARPES and DFT+U data, Figure 3 displays a comparison of (k_x, k_y) cuts. For the low energy band labeled P $3p_z$, we plot the band energy relative to the band minmium at $E - E_F = -8.0$ eV. For the ARPES data, this is deduced by a maximum finding routine within an adequate energy interval, i.e., the maximum of the curvature is plotted. Excellent agreement of the band dispersions in the ARPES and DFT data is found (Figure 3c,f). The hexagonal symmetry of the surface Brillouin zone is also apparent. Since more bands are involved at higher energy, we plot the ARPES intensity at selected energy $E - E_F$ within a small energy interval of ±50 meV (Figure 3a,b). These plots are compared with the band energies of the DFT+U data at the same central energy but within a slightly smaller interval of ±25 meV (Figure 3d,e). This should roughly capture all states that contribute to the ARPES intensity according to the finite energy resolution in experiment. The DFT+U data are additionally color-coded by their energy relative to the central

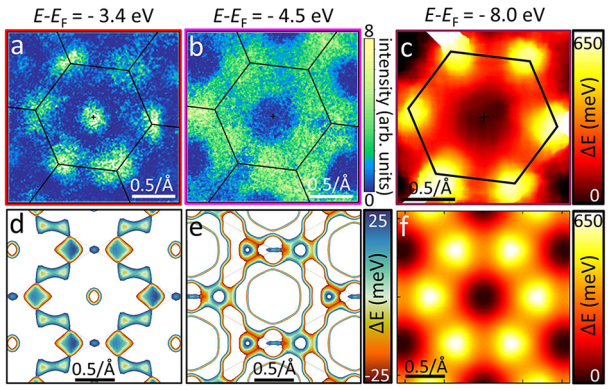

Figure 3. Comparison of (k_x, k_y) plots. (a) Intensity plot of the ARPES curvature integrated over the energy range $E - E_F = -3.4 \pm 0.05$ eV, $T = 43$ K, $h\nu = 50$ eV, 62 layers. (b) Same as (a) at $E - E_F = -4.5 \pm 0.05$ eV. (c) Color plot of the measured band energies for the lowest energy band in Figure 2e,f. The energy ΔE is plotted relative to $E - E_F = -8.0$ eV, $T = 43$ K, $h\nu = 53.5$ eV, and 62 layers. The 2D BZ boundaries are overlaid as black lines in (a)−(c). The selected $E - E_F$ of (a)−(c) are also marked as colored lines between Figure 2e,f. (d) Calculated band energies in the energy interval $E - E_F = -3.4 \pm 0.025$ eV. The band energies relative to $E - E_F = -3.4$ eV are plotted as colors. (e) Same as for (d) for $E - E_F = -4.5 \pm 0.025$ eV with energies plotted relative to $E - E_F = -4.5$ eV. (f) Color plot of the calculated energies for the lowest energy band in Figure 2d,g relative to $E - E_F = -8.0$ eV.

$E - E_F$. Again, one finds a convincing quantitative agreement between the experiment and theory. This corroborates that our parameters are adequately chosen and that DFT+U is a reasonable approach to describe $MnPS_3$.

Next, we relate our data to our knowledge about the magnetic interactions in $MnPS_3$. The monolayer possesses a D_{3d} point group symmetry with the Mn atom in a trigonal antiprismatic environment of S atoms (Figure 1a). Due to the crystal field splitting, the Mn 3d states ($3d^5$, $S = 5/2$) split into two disentangled subsets that exhibit either odd (d_{xz}, d_{yz}) or even (d_{xy}, $d_{x^2-y^2}$, d_{z^2}) mirror symmetry with respect to the monolayer plane. The d_{z^2} orbital further splits from the even subset, becoming the lowest energy state.

Both the direct exchange and the superexchange mechanisms are crucial to understand the origin of the magnetic exchange couplings J_i. Inelastic neutron scattering via the fitted magnon dispersion[68] and DFT+U studies[57] reveal that the dominant exchange between the Mn atoms is the nearest neighbor exchange J_1 inducing AFM coupling. The second-nearest neighbor coupling J_2 is negligible, and the third-nearest neighbor coupling J_3 is about 1/3 of J_1 also leading to AFM coupling. The main contribution to J_1 originates from the direct exchange mechanism as revealed, e.g., by model Hamiltonians with *ab initio* parametrization.[57] It is mainly caused by the direct overlap between the even orbitals $3d_{xy}$, $3d_{z^2}$ and $3d_{x^2-y^2}$ of neighboring Mn atoms and, to a weaker extent (factor of 5.7 smaller), by overlapping odd orbitals (d_{xz}, d_{yz}).[57] Although the effective direct exchange dominates the coupling strength,[57,69] an additional contribution to J_1 originates from the superexchange path Mn(d)−S(p)−Mn(p) as similarly reported for chromium sulfides (exchange path in Figure 5c of ref 70). The strong hybridization between the S 3p and neighboring Mn 3d states is nicely visible in the orbital-projected band structure within the energy range −4 to −3 eV (Figure 2c, Figure S14). Interestingly, the super-exchange process consists of a strong AFM contribution due to hybridization of the S $3p_z$ with t_{2g} orbitals (neglecting the trigonal distortion and assuming octahedral coordination[57]) and a rather weak FM part via the e_g orbitals. Overall, the direct and indirect (superexchange) mechanism lead to strong AFM J_1.[57]

To illustrate the effect of magnetism on the energy bands across T_N, we start with an oversimplified model assuming atomic energy levels for magnetic and nonmagnetic cases. This established model provides a qualitative understanding of the band alignments and the hybridization. Afterward, we discuss the band changes across T_N observed in the ARPES measurements, comparing them with the AFM Néel and PM phase as modeled by DFT+U.

The atomic model is presented in Figure 4a,b. The bare energy levels of Mn 3d and S 3p are shown in the outer parts.

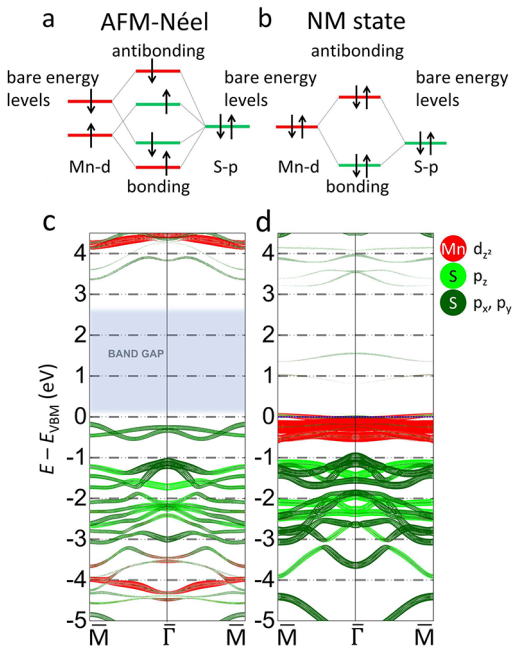

Figure 4. Comparison of magnetic and nonmagnetic (NM) calculations. (a, b) Schematics of the bare and the hybridized atomic orbitals for (a) AFM Néel and (b) NM phase. The atomic Mn 3d levels (red) are either spin-split or not and subsequently hybridize with the S 3p levels (green). Up and down arrows represent the electronic states of the majority and the minority spin-channel in (a), respectively. (c, d) Orbital-projected bulk band structure (E_{VBM}: valence band maximum): (c) AFM Néel phase within DFT+U ($U = 1.8$ eV, same as Figure 2c) and (d) NM phase within DFT calculation ignoring spin degrees of freedom.

With hybridization, we obtain the order of energetic levels, as shown in the center. In the NM phase, the bare energy of the Mn 3d orbitals is above the energy of the S 3p orbitals; therefore, the pd-hybridization produces a bonding state that is mainly S 3p and an antibonding state that is mainly Mn 3d (Figure 4b). This picture is reflected in the calculated band structure of the NM phase, where spin degrees of freedom and Hubbard U parameters are neglected (Figure 4d). The NM phase exhibits bands of pure $3d_{z^2}$ character at $E - E_{VBM} \simeq -0.5$ eV. At slightly higher energies, one finds bands purely from the other even 3d orbitals as expected for the trigonal antiprismatic crystal field (not shown). The Mn 3d bands are all at energies higher than those of the occupied S 3p bands. In the AFM

Néel case, the spin splitting pushes the majority spins of the Mn $3d_{z^2}$ below the S 3p orbitals. Therefore, the hybridization of the majority spins produces a bonding state that is mainly Mn $3d_{z^2}$-type and an antibonding state that is mainly S 3p (Figure 4a). This, in turn, is visible in the calculated AFM Néel band structure (Figure 4c), where the Mn $3d_{z^2}$ bands appear now 4 eV below and above E_F, falling into the valence and conduction bands, respectively. The level order of the majority spin-channel with respect to the S 3p bands, thus, is opposite to the order in the NM case.

One can also see that the orbital character of these bands is significantly mixed in the AFM case as expected for hybridization (see also Figure 2c. The participation of S 3p and Mn 3d orbitals in the same band, moreover, indicates the involvement of superexchange processes in the AFM ordering (Supplementary Section S7). Finally, the presence of the Mn-d bands at E_F in the NM case strongly promotes interaction effects, i.e., the strong Coulomb interaction within the narrow d bands and the half-filled condition x (Mn d^5 configuration) favor the insulating Mott state even at high temperature.

The experimental changes of the electronic band structure with temperature T are shown in Figure 5, i.e., ARPES data above and below T_N recorded at the identical spot of the sample. They are displayed along the $\overline{M\Gamma M}$ direction (Figure 5b,c) and as (k_x, k_y) cuts through the band dominated by the Mn $3d_{z^2}$ orbitals (Figure 5e–h). ARPES data at additional T values are presented in Supplementary Section S3. Most striking is the apparent splitting of the Mn $3d_{z^2}$ band in the central region around $\bar{\Gamma}$, that disappears above T_N. Accordingly, the energy maximum of the upper band shifts from $\bar{\Gamma}$ toward $|k_{\|}| \simeq 0.25$/Å. These band changes reappear in the (k_x, k_y) cuts displayed at an energy slightly below the maxima. A circle of missing intensity in the BZ center is found below $T_N = 78$ K (Figure 5e,f) and a ring of reduced intensity is found above T_N (Figure 5g,h). The largely hexagonal symmetry is preserved below T_N as expected for the AFM Néel phase with primitive magnetic cell commensurate with the structural cell.[55] There are additional, more subtle changes between Figure 5b,c. First, the curvature of the P $3p_z$ band at the lowest energy changes. Second, the two branches declining with $|k_{\|}|$ at $E - E_F \simeq -3.6$ eV largely disappear above T_N, and the corresponding upper band at $E - E_F \simeq -3.1$ eV appears more flat. These changes are reproduced in several cool-downs for distinct flakes with different thicknesses and are also observed in the raw data (Supplementary Figures S6f–g, S9e). Hence, also the S 3p bands change across T_N plausibly, indicating the involvement of superexchange. To model the ARPES data above T_N, we calculate the PM phase within the DFT+U approach (Supplementary Section S2). It is a disordered magnetic state, where each spin fluctuates randomly and rapidly without any correlation to its neighbors. The PM calculation shows d_{z^2} levels over a wider energy range, whereas the AFM Néel phase exhibits two distinct d_{z^2} peaks (Figure 5a,d). Thus, the leading change of the Mn 3d bands across T_N is reproduced, while not the details. Note that also the distribution of S 3p levels changes across T_N corroborating their involvement in the magnetic structure.

We have demonstrated the first successful ARPES study of exfoliated magnetic 2D materials using rather inert $MnPS_3$. We find good agreement with DFT+U calculations, if the selection rules imposed by the photon beam geometry are adequately taken into account. This, in turn, enables the U parameter to be determined. It is $U = 1.8$ eV. Moreover, it enables to

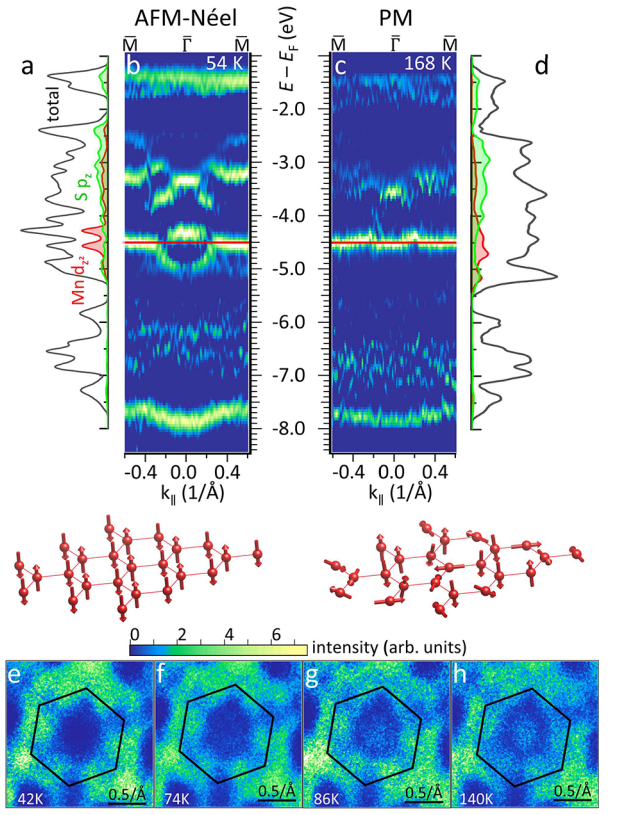

Figure 5. Comparison between AFM-Néel and PM phases. (a) Density of states (black, integrated over the whole BZ) and orbital contributions from Mn $3d_{z^2}$ (red) and S $3p_z$ (green) orbitals for the calculated AFM Néel phase sketched below. (b, c) Curvature plots of ARPES data measured at the same sample spot for the temperatures marked ($T_N = 78$ K), $h\nu = 50$ *eV*, 62 layers. (d) Same as (a) for the PM phase with spin configuration sketched below. The energy scale in the center is valid for (a)–(d). (e–h) Intensity plots of ARPES curvature in the (k_x, k_y) plane recorded at the same sample spot at varying T values as marked, $E - E_F = -4.5 \pm 0.05$ eV as indicated in (b and (c), $h\nu = 50$ eV, 13 layers. The 2D BZ of $MnPS_3$ is overlaid (black hexagon). These data are recorded on a different flake than the data in Figure 3b (different beam geometry), which likely leads to the slightly different intensity distribution.

identify the orbital character of the observed bands. Cooling below the Néel temperature, we find pronounced changes of bands that are dominated by Mn 3d orbitals, but hybridized with S 3p orbitals, and smaller changes for bands with dominating S 3p character, but hybridized with Mn 3d levels. Comparing DFT+U data of the antiferromagnetic and paramagnetic phase reproduces the changes qualitatively. A very similar band structure is observed down to the monolayer with minor changes that appear both in experiments and calculation. The large variety of MPX_3 materials (M = Mn, Ni, Fe, Co, Zn; X = S, Se) as well as corresponding alloys[57,69] with multiple magnetic and magnetoelectric configurations[71] opens a vast field for studying band structure changes across the critical temperature. This will enable a more concise understanding of the interrelation between magnetism and the electronic structure for these novel types of 2D magnets.

Details on sample preparation, flake characterization (AFM , Raman, XPS), additional ARPES experiments, and additional DFT calculations, in particular the adaption of U and k_z for comparison of DFT ARPES data, analysis of the orbital projections of bands for the PM, NM, and AFM cases, additional ARPES data regarding T and $h\nu$ dependence as well as ARPES data obtained on a rough substrate and indicating the influence of strain (PDF)

AUTHOR INFORMATION

Corresponding Author

Markus Morgenstern − *II. Institute of Physics B and JARA-FIT, RWTH-Aachen University, 52074 Aachen, Germany;* orcid.org/0000-0002-3993-6880; Email: mmorgens@physik.rwth-aachen.de

Authors

Jeff Strasdas − *II. Institute of Physics B and JARA-FIT, RWTH-Aachen University, 52074 Aachen, Germany*

Benjamin Pestka − *II. Institute of Physics B and JARA-FIT, RWTH-Aachen University, 52074 Aachen, Germany*

Miłosz Rybak − *Department of Semiconductor Materials Engineering, Faculty of Fundamental Problems of Technology, Wrocław University of Science and Technology, 50-370 Wrocław, Poland*

Adam K. Budniak − *Schulich Faculty of Chemistry, Solid State Institute, Russell Berrie Nanotechnology Institute and Helen Diller Quantum Center, Technion − Israel Institute of Technology, Haifa 3200003, Israel*

Niklas Leuth − *II. Institute of Physics B and JARA-FIT, RWTH-Aachen University, 52074 Aachen, Germany*

Honey Boban − *Peter Grünberg Institute (PGI-6), Forschungszentrum Jülich, Jülich 52428, Germany*

Vitaliy Feyer − *Peter Grünberg Institute (PGI-6), Forschungszentrum Jülich, Jülich 52428, Germany;* orcid.org/0000-0002-7104-5420

Iulia Cojocariu − *Peter Grünberg Institute (PGI-6), Forschungszentrum Jülich, Jülich 52428, Germany*

Daniel Baranowski − *Peter Grünberg Institute (PGI-6), Forschungszentrum Jülich, Jülich 52428, Germany*

José Avila − *Synchrotron-SOLEIL, Université Paris-Saclay, Paris F91192, France*

Pavel Dudin − *Synchrotron-SOLEIL, Université Paris-Saclay, Paris F91192, France*

Aaron Bostwick − *Advanced Light Source, Lawrence Berkeley National Laboratory, Berkeley, California 94720, United States*

Chris Jozwiak − *Advanced Light Source, Lawrence Berkeley National Laboratory, Berkeley, California 94720, United States;* orcid.org/0000-0002-0980-3753

Eli Rotenberg − *Advanced Light Source, Lawrence Berkeley National Laboratory, Berkeley, California 94720, United States;* orcid.org/0000-0002-3979-8844

Carmine Autieri − *International Research Centre MagTop, Institute of Physics, Polish Academy of Sciences, PL-02668 Warsaw, Poland*

Yaron Amouyal − *Department of Materials Science and Engineering, Technion − Israel Institute of Technology, Haifa 3200003, Israel;* orcid.org/0000-0003-2198-3539

Lukasz Plucinski − *Peter Grünberg Institute (PGI-6), Forschungszentrum Jülich, Jülich 52428, Germany*

Efrat Lifshitz − *Schulich Faculty of Chemistry, Solid State Institute, Russell Berrie Nanotechnology Institute and Helen Diller Quantum Center, Technion − Israel Institute of Technology, Haifa 3200003, Israel*

Magdalena Birowska − *Institute of Theoretical Physics, Faculty of Physics, University of Warsaw, 02-093 Warsaw, Poland;* orcid.org/0000-0001-6357-7913

Notes

The authors declare no competing financial interest.

ACKNOWLEDGMENTS

We thank Xiao Hou and Mohammed Qahosh for their support during the measurements at ALS and Elettra, respectively. We acknowledge financial support from the German Research Foundation (DFG) via the project Mo 858/19-1, from the European Union's Horizon 2020 research and innovation program under Grant Agreement Number 881603 (Graphene Flagship, Core 3), and from the German Ministry of Education and Research (Project 05K2022 -ioARPES). M.B. acknowledges support from the University of Warsaw within the project "Excellence Initiative-Research University" program. We acknowledge Polish high-performance computing infrastructure PLGrid for awarding this project access to the LUMI supercomputer, owned by the EuroHPC Joint Undertaking, hosted by CSC (Finland) and the LUMI consortium through PLL/2022/03/016435. We acknowledge access to the Nano-ESCA beamline of Elettra, the Italian synchrotron facility, the Maestro beamline of ALS, the American synchrotron facility, and the Antares beamline of Soleil, the French synchrotron facility. E.L. is supported by the Israel Science Foundation (Project No. 2528/19) and by the Deutsche - Israel Program (Project No. NA1223/2-1). A.K.B. and E.L. were supported by the European Commission via the Marie-Sklodowska Curie action Phonsi (H2020-MSCA-ITN-642656). C.A. is supported by the Foundation for Polish Science through the International Research Agendas program cofinanced by the European Union within the Smart Growth Operational Programme (Grant No. MAB/2017/1). H.B. and L.P. were supported by the DFG via the Project PL 712/5-1.

REFERENCES

(1) Huang, B.; Clark, G.; Navarro-Moratalla, E.; Klein, D. R.; Cheng, R.; Seyler, K. L.; Zhong, D.; Schmidgall, E.; McGuire, M. A.; Cobden, D. H.; Yao, W.; Xiao, D.; Jarillo-Herrero, P.; Xu, X. Layer-dependent ferromagnetism in a van der Waals crystal down to the monolayer limit. *Nature* **2017**, *546*, 270.

(2) Gong, C.; Li, L.; Li, Z.; Ji, H.; Stern, A.; Xia, Y.; Cao, T.; Bao, W.; Wang, C.; Wang, Y.; Qiu, Z. Q.; Cava, R. J.; Louie, S. G.; Xia, J.; Zhang, X. Discovery of intrinsic ferromagnetism in two-dimensional van der Waals crystals. *Nature* **2017**, *546*, 265.

(3) Huang, B.; McGuire, M. A.; May, A. F.; Xiao, D.; Jarillo-Herrero, P.; Xu, X. Emergent phenomena and proximity effects in two-dimensional magnets and heterostructures. *Nat. Mater.* **2020**, *19*, 1276.

(4) Gibertini, M.; Koperski, M.; Morpurgo, A. F.; Novoselov, K. S. Magnetic 2D materials and heterostructures. *Nat. Nanotechnol.* **2019**, *14*, 408.

(5) Gong, C.; Zhang, X. Two-dimensional magnetic crystals and emergent heterostructure devices. *Science* **2019**, *363*, 706.

(6) Burch, K. S.; Mandrus, D.; Park, J.-G. Magnetism in two-dimensional van der Waals materials. *Nature* **2018**, *563*, 47.

(7) Fei, Z.; Huang, B.; Malinowski, P.; Wang, W.; Song, T.; Sanchez, J.; Yao, W.; Xiao, D.; Zhu, X.; May, A. F.; Wu, W.; Cobden, D. H.; Chu, J.-H.; Xu, X. Two-dimensional itinerant ferromagnetism in atomically thin Fe3GeTe2. *Nat. Mater.* **2018**, *17*, 778.
(8) Novoselov, K. S.; Mishchenko, A.; Carvalho, A.; Castro Neto, A. H. 2D materials and van der Waals heterostructures. *Science* **2016**, *353*, aac9439.
(9) Huang, B.; Clark, G.; Klein, D. R.; MacNeill, D.; Navarro-Moratalla, E.; Seyler, K. L.; Wilson, N.; McGuire, M. A.; Cobden, D. H.; Xiao, D.; Yao, W.; Jarillo-Herrero, P.; Xu, X. Electrical control of 2D magnetism in bilayer CrI3. *Nat. Nanotechnol.* **2018**, *13*, 544.
(10) Jiang, S.; Shan, J.; Mak, K. F. Electric-field switching of two-dimensional van der Waals magnets. *Nat. Mater.* **2018**, *17*, 406.
(11) Jiang, S.; Li, L.; Wang, Z.; Mak, K. F.; Shan, J. Controlling magnetism in 2D CrI3 by electrostatic doping. *Nat. Nanotechnol.* **2018**, *13*, 549.
(12) Deng, Y.; Yu, Y.; Song, Y.; Zhang, J.; Wang, N. Z.; Sun, Z.; Yi, Y.; Wu, Y. Z.; Wu, S.; Zhu, J.; Wang, J.; Chen, X. H.; Zhang, Y. Gate-tunable room-temperature ferromagnetism in two-dimensional Fe3GeTe2. *Nature* **2018**, *563*, 94.
(13) Sierra, J. F.; Fabian, J.; Kawakami, R. K.; Roche, S.; Valenzuela, S. O. Van der Waals heterostructures for spintronics and opto-spintronics. *Nat. Nanotechnol.* **2021**, *16*, 856.
(14) Wu, Y.; Yin, G.; Pan, L.; Grutter, A. J.; Pan, Q.; Lee, A.; Gilbert, D. A.; Borchers, J. A.; Ratcliff, W.; Li, A.; Han, X.; Wang, K. L. Large exchange splitting in monolayer graphene magnetized by an antiferromagnet. *Nat. Electron.* **2020**, *3*, 604.
(15) Ghiasi, T. S.; Kaverzin, A. A.; Dismukes, A. H.; de Wal, D. K.; Roy, X.; van Wees, B. J. Electrical and thermal generation of spin currents by magnetic bilayer graphene. *Nat. Nanotechnol.* **2021**, *16*, 788.
(16) Tang, C.; Zhang, Z.; Lai, S.; Tan, Q.; Gao, W. Magnetic Proximity Effect in Graphene/CrBr 3 van der Waals Heterostructures. *Adv. Mater.* **2020**, *32*, No. 1908498.
(17) Zhong, D.; Seyler, K. L.; Linpeng, X.; Wilson, N. P.; Taniguchi, T.; Watanabe, K.; McGuire, M. A.; Fu, K.-M. C.; Xiao, D.; Yao, W.; Xu, X. Layer-resolved magnetic proximity effect in van der Waals heterostructures. *Nat. Nanotechnol.* **2020**, *15*, 187.
(18) Zhao, W.; Fei, Z.; Song, T.; Choi, H. K.; Palomaki, T.; Sun, B.; Malinowski, P.; McGuire, M. A.; Chu, J.-H.; Xu, X.; Cobden, D. H. Magnetic proximity and nonreciprocal current switching in a monolayer WTe2 helical edge. *Nat. Mater.* **2020**, *19*, 503.
(19) Kang, K.; Jiang, S.; Berger, H.; Watanabe, K.; Taniguchi, T.; Forró, L.; Shan, J.; Mak, K. F. Giant anisotropic magnetoresistance in Ising superconductor-magnetic insulator tunnel junctions. *ArXiv (Superconductivity)*, 2021, 2101.01327, https://arxiv.org/abs/2101.01327 (accessed November 7, 2022).
(20) Hamill, A.; Heischmidt, B.; Sohn, E.; Shaffer, D.; Tsai, K.-T.; Zhang, X.; Xi, X.; Suslov, A.; Berger, H.; Forró, L.; Burnell, F. J.; Shan, J.; Mak, K. F.; Fernandes, R. M.; Wang, K.; Pribiag, V. S. Two-fold symmetric superconductivity in few-layer NbSe2. *Nat. Phys.* **2021**, *17*, 949.
(21) Kezilebieke, S.; Huda, M. N.; Vaňo, V.; Aapro, M.; Ganguli, S. C.; Silveira, O. J.; Głodzik, S.; Foster, A. S.; Ojanen, T.; Liljeroth, P. Topological superconductivity in a van der Waals heterostructure. *Nature* **2020**, *588*, 424.
(22) Xie, H.; Luo, X.; Ye, G.; Ye, Z.; Ge, H.; Sung, S. H.; Rennich, E.; Yan, S.; Fu, Y.; Tian, S.; Lei, H.; Hovden, R.; Sun, K.; He, R.; Zhao, L. Twist engineering of the two-dimensional magnetism in double bilayer chromium triiodide homostructures. *Nat. Phys.* **2022**, *18*, 30.
(23) Song, T.; Sun, Q.-C.; Anderson, E.; Wang, C.; Qian, J.; Taniguchi, T.; Watanabe, K.; McGuire, M. A.; Stöhr, R.; Xiao, D.; Cao, T.; Wrachtrup, J.; Xu, X. Direct visualization of magnetic domains and moiré magnetism in twisted 2D magnets. *Science* **2021**, *374*, 1140.
(24) Xu, Y.; Ray, A.; Shao, Y.-T.; Jiang, S.; Lee, K.; Weber, D.; Goldberger, J. E.; Watanabe, K.; Taniguchi, T.; Muller, D. A.; Mak, K. F.; Shan, J. Coexisting ferromagnetic−antiferromagnetic state in twisted bilayer CrI3. *Nat. Nanotechnol.* **2022**, *17*, 143.
(25) Momma, K.; Izumi, F. VESTA3 for three-dimensional visualization of crystal, volumetric and morphology data. *J. Appl. Crystallogr.* **2011**, *44*, 1272.
(26) Moser, S. An experimentalists guide to the matrix element in angle resolved photoemission. *J. Electr. Spectr. Rel. Phen.* **2017**, *214*, 29.
(27) Watson, M. D.; Marković, I.; Mazzola, F.; Rajan, A.; Morales, E. A.; Burn, D. M.; Hesjedal, T.; van der Laan, G.; Mukherjee, S.; Kim, T. K.; Bigi, C.; Vobornik, I.; Ciomaga Hatnean, M.; Balakrishnan, G.; King, P. D. C. Direct observation of the energy gain underpinning ferromagnetic superexchange in the electronic structure of $CrGeTe_3$. *Phys. Rev. B* **2020**, *101*, No. 205125.
(28) Yilmaz, T.; Geilhufe, R. M.; Pletikosić, I.; Fernando, G. W.; Cava, R. J.; Valla, T.; Vescovo, E.; Sinkovic, B. Multi-hole bands and quasi−two-dimensionality in Cr_2 Ge_2 Te_6 studied by angle-resolved photoemission spectroscopy. *Europhys. Lett.* **2021**, *133*, No. 27002.
(29) Xu, X.; Li, Y. W.; Duan, S. R.; Zhang, S. L.; Chen, Y. J.; Kang, L.; Liang, A. J.; Chen, C.; Xia, W.; Xu, Y.; Malinowski, P.; Xu, X. D.; Chu, J.-H.; Li, G.; Guo, Y. F.; Liu, Z. K.; Yang, L. X.; Chen, Y. L. Signature for non-Stoner ferromagnetism in the van der Waals ferromagnet Fe_3GeTe_2. *Phys. Rev. B* **2020**, *101*, No. 201104.
(30) Liu, J. S.; Huan, S. C.; Liu, Z. H.; Liu, W. L.; Liu, Z. T.; Lu, X. L.; Huang, Z.; Jiang, Z. C.; Wang, X.; Yu, N.; Zou, Z. Q.; Guo, Y. F.; Shen, D. W. Electronic structure of the high-mobility two-dimensional antiferromagnetic metal $GdTe_3$. *Phys. Rev. Mater.* **2020**, *4*, No. 114005.
(31) Li, Y. F.; Wang, W.; Guo, W.; Gu, C. Y.; Sun, H. Y.; He, L.; Zhou, J.; Gu, Z. B.; Nie, Y. F.; Pan, X. Q. Electronic structure of ferromagnetic semiconductor $CrGeTe_3$ by angle-resolved photoemission spectroscopy. *Phys. Rev. B* **2018**, *98*, No. 125127.
(32) Suzuki, M.; Gao, B.; Koshiishi, K.; Nakata, S.; Hagiwara, K.; Lin, C.; Wan, Y. X.; Kumigashira, H.; Ono, K.; Kang, S.; Kang, S.; Yu, J.; Kobayashi, M.; Cheong, S.-W.; Fujimori, A. Coulomb-interaction effect on the two-dimensional electronic structure of the van der Waals ferromagnet $Cr_2Ge_2Te_6$. *Phys. Rev. B* **2019**, *99*, No. 161401.
(33) Zhang, Y.; Lu, H.; Zhu, X.; Tan, S.; Feng, W.; Liu, Q.; Zhang, W.; Chen, Q.; Liu, Y.; Luo, X.; Xie, D.; Luo, L.; Zhang, Z.; Lai, X. Emergence of Kondo lattice behavior in a van der Waals itinerant ferromagnet, Fe_3 $GeTe_2$. *Sci. Adv.* **2018**, *4*, No. aao6791.
(34) Kong, T.; Stolze, K.; Timmons, E. I.; Tao, J.; Ni, D.; Guo, S.; Yang, Z.; Prozorov, R.; Cava, R. J. VI_3 - a New Layered Ferromagnetic Semiconductor. *Adv. Mater.* **2019**, *31*, No. 1808074.
(35) Jiang, W.; Yang, Z.; Li, Y.; Wang, G.; Jing, Q.; Guan, D.; Ma, J.; Zhang, W.; Qian, D. Spin-split valence bands of the ferromagnetic insulator Cr2Ge2Te6 studied by angle-resolved photoemission spectroscopy. *J. Appl. Phys.* **2020**, *127*, No. 023901.
(36) Voloshina, E.; Jin, Y.; Dedkov, Y. ARPES studies of the ground state electronic properties of the van der Waals transition metal trichalcogenide $CoPS_3$. *Chem. Phys. Lett.* **2023**, *823*, No. 140511.
(37) Zhang, X.; Lu, Q.; Liu, W.; Niu, W.; Sun, J.; Cook, J.; Vaninger, M.; Miceli, P. F.; Singh, D. J.; Lian, S.-W.; Chang, T.-R.; He, X.; Du, J.; He, L.; Zhang, R.; Bian, G.; Xu, Y. Room-temperature intrinsic ferromagnetism in epitaxial $CrTe_2$ ultrathin films. *Nat. Commun.* **2021**, *12*, 2492.
(38) Joy, P. A.; Vasudevan, S. Magnetism in the layered transition-metal thiophosphates MPS_3 (M = Mn, Fe, and Ni). *Phys. Rev. B* **1992**, *46*, No. 5425.
(39) Susner, M. A.; Chyasnavichyus, M.; McGuire, M. A.; Ganesh, P.; Maksymovych, P. Metal Thio- and Selenophosphates as Multifunctional van der Waals Layered Materials. *Adv. Mater.* **2017**, *29*, No. 1602852.
(40) Wang, F.; Shifa, T. A.; Yu, P.; He, P.; Liu, Y.; Wang, F.; Wang, Z.; Zhan, X.; Lou, X.; Xia, F.; He, J. New Frontiers on van der Waals Layered Metal Phosphorous Trichalcogenides. *Adv. Funct. Mater.* **2018**, *28*, No. 1802151.

(41) Kamata, A.; Noguchi, K.; Suzuki, K.; Tezuka, H.; Kashiwakura, T.; Ohno, Y.; Nakai, S. Resonant 2p →3d Photoemission Measurement of MPS_3 (M = Mn, Fe, Ni). *J. Phys. Soc. Jpn.* **1997**, *66*, 401.
(42) Bianchi, M.; Acharya, S.; Dirnberger, F.; Klein, J.; Pashov, D.; Mosina, K.; Sofer, Z.; Rudenko, A. N.; Katsnelson, M. I.; van Schilfgaarde, M.; Rösner, M.; Hofmann, P. Paramagnetic Electronic Structure of CrSBr: Comparison between Ab Initio GW Theory and Angle-Resolved Photoemission Spectroscopy. *ArXiv (Strongly Correlated Electrons)*, 2023, 2303.01292, https://arxiv.org/abs/2303.01292 (accessed May 15, 2023).
(43) Vaclavkova, D.; Delhomme, A.; Faugeras, C.; Potemski, M.; Bogucki, A.; Suffczyński, J.; Kossacki, P.; Wildes, A. R.; Grémaud, B.; Saúl, A. Magnetoelastic interaction in the two-dimensional magnetic material $MnPS_3$ studied by first principles calculations and Raman experiments. *2D Mater.* **2020**, *7*, No. 035030.
(44) Liu, S.; Granados del Águila, A.; Bhowmick, D.; Gan, C. K.; Thu Ha Do, T.; Prosnikov, M. A.; Sedmidubský, D.; Sofer, Z.; Christianen, P. C. M.; Sengupta, P.; Xiong, Q. Direct Observation of Magnon-Phonon Strong Coupling in Two-Dimensional Antiferromagnet at High Magnetic Fields. *Phys. Rev. Lett.* **2021**, *127*, No. 097401.
(45) Ressouche, E.; Loire, M.; Simonet, V.; Ballou, R.; Stunault, A.; Wildes, A. Magnetoelectric $MnPS_3$ as a candidate for ferrotoroidicity. *Phys. Rev. B* **2010**, *82*, No. 100408.
(46) Lai, Y.; Song, Z.; Wan, Y.; Xue, M.; Wang, C.; Ye, Y.; Dai, L.; Zhang, Z.; Yang, W.; Du, H.; Yang, J. Two-dimensional ferromagnetism and driven ferroelectricity in van der Waals $CuCrP_2$ S_6. *Nanoscale* **2019**, *11*, 5163.
(47) Chu, H.; Roh, C. J.; Island, J. O.; Li, C.; Lee, S.; Chen, J.; Park, J.-G.; Young, A. F.; Lee, J. S.; Hsieh, D. Linear Magnetoelectric Phase in Ultrathin $MnPS_3$ Probed by Optical Second Harmonic Generation. *Phys. Rev. Lett.* **2020**, *124*, No. 027601.
(48) Kim, S. Y.; Kim, T. Y.; Sandilands, L. J.; Sinn, S.; Lee, M.-C.; Son, J.; Lee, S.; Choi, K.-Y.; Kim, W.; Park, B.-G.; Jeon, C.; Kim, H.-D.; Park, C.-H.; Park, J.-G.; Moon, S.; Noh, T. Charge-Spin Correlation in van der Waals Antiferromagnet $NiPS_3$. *Phys. Rev. Lett.* **2018**, *120*, No. 136402.
(49) Kang, S.; Kim, K.; Kim, B. H.; Kim, J.; Sim, K. I.; Lee, J.-U.; Lee, S.; Park, K.; Yun, S.; Kim, T.; Nag, A.; Walters, A.; Garcia-Fernandez, M.; Li, J.; Chapon, L.; Zhou, K.-J.; Son, Y.-W.; Kim, J. H.; Cheong, H.; Park, J.-G. Coherent many-body exciton in van der Waals antiferromagnet $NiPS_3$. *Nature* **2020**, *583*, 785.
(50) Ergeçen, E.; Ilyas, B.; Mao, D.; Po, H. C.; Yilmaz, M. B.; Kim, J.; Park, J.-G.; Senthil, T.; Gedik, N. Magnetically brightened dark electron-phonon bound states in a van der Waals antiferromagnet. *Nat. Commun.* **2022**, *13*, 98 DOI: 10.1038/s41467-021-27741-3.
(51) Birowska, M.; Faria Junior, P. E.; Fabian, J.; Kunstmann, J. Large exciton binding energies in $MnPS_3$ as a case study of a van der Waals layered magnet. *Phys. Rev. B* **2021**, *103*, No. L121108.
(52) Hwangbo, K.; Zhang, Q.; Jiang, Q.; Wang, Y.; Fonseca, J.; Wang, C.; Diederich, G. M.; Gamelin, D. R.; Xiao, D.; Chu, J.-H.; Yao, W.; Xu, X. Highly anisotropic excitons and multiple phonon bound states in a van der Waals antiferromagnetic insulator. *Nat. Nanotechnol.* **2021**, *16*, 655.
(53) Dirnberger, F.; Bushati, R.; Datta, B.; Kumar, A.; MacDonald, A. H.; Baldini, E.; Menon, V. M. Spin-correlated exciton−polaritons in a van der Waals magnet. *Nat. Nanotechnol.* **2022**, *17*, 1060.
(54) Belvin, C. A.; Baldini, E.; Ozel, I. O.; Mao, D.; Po, H. C.; Allington, C. J.; Son, S.; Kim, B. H.; Kim, J.; Hwang, I.; Kim, J. H.; Park, J.-G.; Senthil, T.; Gedik, N. Exciton-driven antiferromagnetic metal in a correlated van der Waals insulator. *Nat. Commun.* **2021**, *12*, 4837.
(55) Kurosawa, K.; Saito, S.; Yamaguchi, Y. Neutron Diffraction Study on $MnPS_3$ and $FePS_3$. *J. Phys. Soc. Jpn.* **1983**, *52*, No. 3919.
(56) Brec, R. Review on structural and chemical properties of transition metal phosphorous trisulfides MPS_3. *Solid State Ionics* **1986**, *22*, 3.
(57) Autieri, C.; Cuono, G.; Noce, C.; Rybak, M.; Kotur, K. M.; Agrapidis, C. E.; Wohlfeld, K.; Birowska, M. Limited Ferromagnetic Interactions in Monolayers of MPS_3 (M = Mn and Ni). *J. Phys. Chem. C* **2022**, *126*, 6791.
(58) Lim, S. Y.; Kim, K.; Lee, S.; Park, J.-G.; Cheong, H. Thickness dependence of antiferromagnetic phase transition in Heisenberg-type $MnPS_3$. *Current Appl. Phys.* **2021**, *21*, 1.
(59) Kim, K.; Lim, S. Y.; Kim, J.; Lee, J.-U.; Lee, S.; Kim, P.; Park, K.; Son, S.; Park, C.-H.; Park, J.-G.; Cheong, H. Antiferromagnetic ordering in van der Waals 2D magnetic material $MnPS_3$ probed by Raman spectroscopy. *2D Mater.* **2019**, *6*, No. 041001.
(60) Long, G.; Henck, H.; Gibertini, M.; Dumcenco, D.; Wang, Z.; Taniguchi, T.; Watanabe, K.; Giannini, E.; Morpurgo, A. F. Persistence of Magnetism in Atomically Thin $MnPS_3$ Crystals. *Nano Lett.* **2020**, *20*, 2452.
(61) Babuka, T.; Makowska-Janusik, M.; Peschanskii, A.; Glukhov, K.; Gnatchenko, S.; Vysochanskii, Y. Electronic and vibrational properties of pure $MnPS_3$ crystal: Theoretical and experimental investigation. *Comput. Mater. Sci.* **2020**, *177*, No. 109592.
(62) Ni, Z.; Zhang, H.; Hopper, D. A.; Haglund, A. V.; Huang, N.; Jariwala, D.; Bassett, L. C.; Mandrus, D. G.; Mele, E. J.; Kane, C. L.; Wu, L. Direct Imaging of Antiferromagnetic Domains and Anomalous Layer-Dependent Mirror Symmetry Breaking in Atomically Thin $MnPS_3$. *Phys. Rev. Lett.* **2021**, *127*, No. 187201.
(63) Shan, J.-Y.; Ye, M.; Chu, H.; Lee, S.; Park, J.-G.; Balents, L.; Hsieh, D. Giant modulation of optical nonlinearity by Floquet engineering. *Nature* **2021**, *600*, 235.
(64) Wildes, A. R.; Rønnow, H. M.; Roessli, B.; Harris, M. J.; Godfrey, K. W. Static and dynamic critical properties of the quasi-two-dimensional antiferromagnet MnPS3. *Phys. Rev. B* **2006**, *74*, No. 094422.
(65) Grasso, V.; Neri, F.; Perillo, P.; Silipigni, L.; Piacentini, M. Optical-absorption spectra of crystal-field transitions in $MnPS_3$ at low temperatures. *Phys. Rev. B* **1991**, *44*, No. 11060.
(66) Du, K.-Z.; Wang, X.-Z.; Liu, Y.; Hu, P.; Utama, M. I. B.; Gan, C. K.; Xiong, Q.; Kloc, C. Weak Van der Waals Stacking, Wide-Range Band Gap, and Raman Study on Ultrathin Layers of Metal Phosphorus Trichalcogenides. *ACS Nano* **2016**, *10*, 1738.
(67) Wiemann, C.; Patt, M.; Krug, I. P.; Weber, N. B.; Escher, M.; Merkel, M.; Schneider, C. M. A New Nanospectroscopy Tool with Synchrotron Radiation: NanoESCA@Elettra, e-J. *Surf. Sci. Nanotechnol.* **2011**, *9*, 395.
(68) Wildes, A. R.; Roessli, B.; Lebech, B.; Godfrey, K. W. Spin waves and the critical behaviour of the magnetization in $MnPS_3$. *J. Phys.: Cond. Mater.* **1998**, *10*, 6417.
(69) Basnet, R.; Kotur, K. M.; Rybak, M.; Stephenson, C.; Bishop, S.; Autieri, C.; Birowska, M.; Hu, J. Controlling magnetic exchange and anisotropy by nonmagnetic ligand substitution in layered MPX_3(M = Ni, Mn; X = S, Se). *Phys. Rev. Research* **2022**, *4*, No. 023256.
(70) Ushakov, A. V.; Kukusta, D. A.; Yaresko, A. N.; Khomskii, D. I. Magnetism of layered chromium sulfides $MCRS_2$ (M= Na, K, Ag, and Au): A first-principles study. *Phys. Rev. B* **2013**, *87*, No. 014418.
(71) Grasso, V.; Silipigni, L. Low-dimensional materials: The MPX_3 family, physical features and potential future applications. *Riv. Nuov. Cim.* **2002**, *25*, 1.